International Journal of Multiphase Flow 36 (2010) 324–332

Contents lists available at ScienceDirect

International Journal of Multiphase Flow

journal homepage: www.elsevier.com/locate/ijmulflow

Measurement of inertial particle clustering and relative velocity statistics in isotropic turbulence using holographic imaging

J. de Jong [a], J.P.L.C. Salazar [b], S.H. Woodward [a], L.R. Collins [b], H. Meng [a,*]

[a] Mechanical and Aerospace Engineering Department, University at Buffalo, Buffalo, NY 14260, United States
[b] Sibley School of Mechanical and Aerospace Engineering, Cornell University, Ithaca, NY 14853, United States

ARTICLE INFO

Article history:
Received 15 August 2008
Received in revised form 29 July 2009
Accepted 11 November 2009
Available online 26 November 2009

Keywords:
Holographic PIV
Radial distribution function
Collision rate
Isotropic turbulence
Particle statistics
Particle–turbulence interaction

ABSTRACT

We present the first measurements of relative velocity statistics of inertial particles in a homogeneous isotropic turbulent flow with three-dimensional holographic particle image velocimetry (holographic PIV). From the measurements we are able to obtain the radial relative velocity probability density function (PDF) conditioned on the interparticle separation distance, for distances on the order of the Kolmogorov length scale. Together with measurements of the three-dimensional radial distribution function (RDF) in our turbulence chamber, these statistics, in principle, can be used to determine interparticle collision rates via the formula derived by Sundaram and Collins (1997). In addition, we show temporal development of the RDF, which reveals the existence of an extended quasi-steady-state regime in our facility. Over this regime the measured two-particle statistics are compared to direct numerical simulations (DNS) with encouraging qualitative agreement. Statistics at the same Reynolds number but different Stokes numbers demonstrate the ability of the experiment to correctly capture the trends associated with particles of different inertia. Our results further indicate that even at moderate Stokes numbers turbulence may enhance collision rates significantly. Such experimental investigations may prove valuable in validating, guiding and refining numerical models of particle dynamics in turbulent flows.

1. Introduction

Collision and coagulation of dilute inertial particles suspended in turbulent flows are of considerable significance to many important industrial applications (e.g. aerosol synthesis of powders, spray combustion, inhalation drug therapy and pneumatic transport of solids) and naturally occurring flows (e.g. cloud formation, aerosol transport in the atmosphere). In each of these processes, the rate at which particles are brought into contact with each other, i.e. the interparticle collision frequency, is a critical variable to model and predict the evolution of the particle size distribution (Shaw, 2003). It is well known that turbulence can enhance the collision frequency, thereby leading to growth (through coalescence and agglomeration) or reduction (through breakup) of the mean particle size (Ramkrishna, 2000). Models of the collision rate in isotropic turbulence have been constructed based on high-resolution direct numerical simulations (DNS) (Collins and Keswani, 2004). However, to date there is limited experimental data available to support these models (Xue et al., 2008). Using state-of-the-art holographic particle image velocimetry (holographic PIV or HPIV) we seek to address this issue and wherever feasible, validate DNS using experimental data. The insights gained from this knowledge will guide and refine the numerical experiments to ensure the relevant physics is accurately captured.

Experimental measurement of inertial particle clustering and relative velocity statistics in isotropic turbulence requires resolution of the full three-dimensional (3D) dense particle field, which has been beyond the reach of past measurement techniques. Previous experimental measurements of 3D particle fields have been limited to sparse particle fields using imaging techniques such as particle tracking velocimetry (PTV) (Ayyalasomayajula et al., 2006; Cowen and Monismith, 1997; Doh et al., 2002; Hoyer et al., 2005; Voth et al., 2002), tomographic particle image velocimetry (Tomo-PIV) (Elsinga et al., 2006), and forward scattering holographic particle imaging (Owen et al., 2002; Pan and Meng, 2003; Xu et al., 2001). The development of a hybrid digital holographic PIV system (Cao et al., 2008; Meng et al., 2004) has greatly facilitated dense 3D particle field measurements. Recent advancements in this technique, along with a method for measuring the turbulence energy dissipation rate and derived quantities in "box turbulence" (de Jong et al., 2009), have enabled the first comparisons of experimentally measured 3D radial distribution functions (RDFs) to DNS under conditions of excellent parametric overlap (Salazar et al., 2008).

---

* Corresponding author. Tel.: +1 716 645 2593; fax: +1 716 645 2883.
E-mail address: huimeng@buffalo.edu (H. Meng).

0301-9322/$ - see front matter © 2009 Elsevier Ltd. All rights reserved.
doi:10.1016/j.ijmultiphaseflow.2009.11.008

The agreement between experiments and simulations was very good. We also compared an alternative measure of clustering called the correlation dimension (Grassberger and Procaccia, 1983), which was used by (Bec et al., 2007) to quantify clustering, and found equally good agreement.

In this paper, we further extend the HPIV system to investigate the particle pair relative velocity statistics and the temporal evolution of the particle field. Our measurements are performed in the same facility as reported in Salazar et al. (2008), albeit with improved turbulence isotropy through refined fan alignment and balancing of the fan rotation rates. Holographic imaging in double-exposure mode is used to obtain particle velocities and thus the particle radial relative velocity PDF, the second statistic contributing to the collision frequency. Furthermore, we investigate if a steady-state or a quasi-steady-state of the particle field can be achieved in this system.

2. Background theory

The statistical mechanical description of the average collision kernel (Sundaram and Collins, 1997; Wang et al., 1998) incorporates two effects: (1) the non-uniform particle concentration owing to their inertial clustering in regions of high-strain or low vorticity (the local accumulation effect) and (2) the relative velocity between two colliding particles (the turbulent transport effect). These are characterized by the radial distribution function (RDF) which is a statistical mechanical description of a particle distribution that captures the departure of the particle field from a uniform distribution and by the probability density function (PDF) of the radial component of the relative velocity between two particles, respectively. For monodisperse particles of diameter σ, the collision frequency per unit volume $[\mathrm{L}^{-3}\ \mathrm{T}]$ can be written as,

$$N_c = 4\pi n^2 \sigma^2 g(\sigma) \int_{-\infty}^{0} (-w_r) P(w_r|\sigma) dw_r, \tag{1}$$

where $g(r)$ is the RDF, n is the number density of the particles, w_r is the radial component of the relative velocity between two particles and $P(w_r|r)$ is the probability density function (PDF) of w_r conditioned on the particle pair separation distance, r. Extensions of the collision kernel to systems of bidisperse (Zaichik et al., 2006; Zhou et al., 2001) and polydisperse (Derevich, 2007) particles size distributions (PSD) yield a similar functional dependence on the unknown parameters, $g(r)$ and w_r. Typically, these parameters have been quantified through the use of direct numerical simulations (DNS) (Reade and Collins, 2000), and it is the goal of this paper to quantify them using holographic measurements.

3. The radial distribution function and edge correction methods

Local accumulation of particles is caused by the inertial mismatch between the denser particles and the lighter carrier fluid. Due to this density mismatch, particles tend to be depleted from high-vorticity regions and accumulate in high-strain regions of the flow (Maxey, 1987). This inertial mismatch is parameterized by the Stokes number, where $St = \tau_p/\tau_\eta$ is the ratio of the particle response time $\tau_p = \rho_p \sigma^2 / 18 \rho_f \upsilon$, to the fluid response time, here chosen as the Kolmogorov time scale, $\tau_\eta = \sqrt{\nu\varepsilon}$, where ρ_p and ρ_f are the density of the particle and fluid, respectively, ν is the kinematic viscosity of the fluid and ε is the turbulent kinetic energy dissipation rate. Inertial clustering, sometimes referred to as preferential concentration, results in a dramatically non-homogeneous particle distribution, particularly at scales below the Kolmogorov length scale $\eta = (\nu^3/\varepsilon)^{1/4}$. The non-uniform particle concentration field is quantified statistically by the RDF. The RDF relates the number of particle pairs found at a separation distance r from a given particle at the origin to the expected number based on a uniform distribution of particles (McQuarrie, 1976). The RDF can be computed from a field of N_p particles by binning particle pairs according to their separation distance and calculating

$$g(r_i) = \frac{N_i/\Delta V_i}{N/V}, \tag{2}$$

where N_i is the number of particle pairs separated by a distance $r_i \pm \Delta r/2$, ΔV_i is the volume of the discrete shell located at r_i, $N = 1/2 N_p (N_p - 1)$ is the total number of pairs and V is the total volume of the system. The subscript i is the discrete index and does not refer to a vector quantity. The properties of the RDF are such that $g(r < \sigma) = 0$ and $g(\infty) = 1$, or in other words particles cannot be located less than one collision diameter apart and at large separation distance the particle field approaches a uniform distribution. Lower-dimensional projections of the 3D RDF can be measured with a light sheet (Wood et al., 2005) or with a fast sampling probe (Saw et al., 2008; Brenguier and Chaumat, 2001); however, as discussed in Holtzer and Collins (2002) (see also Poelma et al., 2007), these measurements potentially suffer from the inherent averaging that accompanies not having the full 3D particle field. Hence it is ideal to utilize a 3D volumetric measurement technique such as HPIV.

Another complication in experimental measurements of the RDF arises from its sensitivity to the size and shape of the volume over which the particle field is measured. Notice that the RDF (Eq. (2)) is normalized by the average pair density in the experimental volume. Because of clustering, the average pair density for a small sample volume will be larger than the corresponding value in the thermodynamic limit $V \to \infty$ (Salazar et al., 2008). Additionally, for smaller sample volumes, edge corrections are needed to account for particles near the boundaries (Hewett, 1982; Lemson and Sanders, 1991; Provenzale et al., 1994; Sharp, 1979).

The default method for edge correction consists of omitting all shells that cross the boundary from the final averaging (Coleman et al., 1988). Although this does not involve assumptions about the underlying distribution of the particle field, it suffers from several shortcomings: (1) for larger particle separations, the number of available pairs used to calculate the RDF is drastically reduced and (2) the maximum possible two-particle separation distance is limited by the radius of the largest sphere that can be enclosed completely within the sample volume. To improve the statistics at the larger particle separations, a periodic assumption can be used, whereby the particle field is reflected across each of the volume boundaries so that, at each particle location, the same number of shells can be used to calculate the RDF. While the periodic assumption overcomes the first limitation, the maximum possible separation distance is still limited to the largest sphere fully enclosed within the sample volume. The assumption also introduces unphysical correlations between particles near the edges of the volume.

The RDF at separation distances up to the maximum two-particle separation distance in the system can be obtained by using the partial volumes of the shells to normalize the particle pair counts. In even the simplest geometries, direct calculation of these partial volumes is non-trivial. For this reason, the partial volumes are often estimated by means of a Monte Carlo scheme, a method routinely used by the astrophysics community for example (Andreani and Cristiani, 1992; Davis and Peebles, 1983; Hamilton, 1993; Jones et al., 2005; Kerscher et al., 2000; Landy and Szalay, 1993; Pons-Borderia et al., 1999). In the Monte Carlo scheme, an additional set of random data points is generated in the volume that allows the actual data to be compared against a uniform distribution of particles. With the introduction of the random data, three different particle pair distributions can be generated, one involving data–data pairs (DD), one with data–random pairs (DR)

and a third with random–random pairs (*RR*). Multiple combinations of these three distributions have been developed in order to estimate the partial shell volumes (Kerscher, 1999; Kerscher et al., 2000).

A performance comparison of the different Monte Carlo estimators (Kerscher et al., 2000) showed that the Landy and Szalay (1993) estimator contains the least bias. This estimator is defined as

$$g(r_i) = \frac{DD(r_i)}{RR(r_i)} - 2\frac{DR(r_i)}{RR(r_i)} + 2, \tag{3}$$

where $DD(r_i) = \frac{P_{DD}(r_i)}{[N_p(N_p-1)]}$, $DR(r_i) = \frac{P_{DR}(r_i)}{N_p N_R}$ and $RR(r_i) = \frac{P_{RR}(r_i)}{[N_R(N_R-1)]}$ with N_P and N_R being the total number of particles and random points in the sample volume, respectively. $P_{IJ}(r_i)$ is the count of particle pairs of type *IJ*, whose separation distance lies within the bin $r_i \pm \Delta r/2$. The drawback of the Monte Carlo estimators is that if the particle seeding density N_P/V is not equal to the particle seeding density in the thermodynamic limit $V \to \infty$, then Eq. (3) will show a bias.

4. The conditional radial relative velocity probability density function

The second statistic in the formula for the collision frequency (see Eq. (1)) is $P(w_r|r)$, which concerns the statistics of the two-particle relative velocity, $\mathbf{w} = \mathbf{v}_2 - \mathbf{v}_1$, where $\mathbf{v}_1$ and $\mathbf{v}_2$ are the individual particle velocities. Of specific interest is the radial component of the relative velocity,

$$w_r = \mathbf{w} \cdot \frac{\mathbf{r}}{r}, \tag{4}$$

with $\mathbf{r}$ being the separation vector between the two particles. DNS results of the radial relative velocity PDF at contact suggest that the PDF is negatively skewed. For low Stokes numbers, the positive tail has a Gaussian distribution, while the negative tail matches an exponential distribution (Wang et al., 2000). At Stokes numbers near unity, however, the PDF shows a higher peak near zero, and a tail that decays more slowly than an exponential distribution.

In comparison with RDF measurements, resolving the velocity PDF at multiple two-particle separation distances requires a larger sample size. Additionally, owing to the need to match particles from different exposures, obtaining the relative velocity PDF requires a higher degree of accuracy in the measurement of the particle position than that required by the RDF.

5. Experimental setup and methods

The experiments were carried out in a zero-mean gaseous turbulence "box" based on the design of Birouk et al. (1996) with a side length of 40 cm with fans placed in each of the eight corners pointing towards the center of the cube (see Fig. 1). This facility produces a stationary homogeneous isotropic turbulence volume located at the center of the cube in which these measurements were conducted. Further details of the flow facility can be found in de Jong et al. (2009).

5.1. Flow characterization

Flow velocity statistics were obtained by particle image velocimetry (PIV) and laser Doppler anemometry (LDA). Details of the approach used to characterize the flow can be found in de Jong et al. (2009). The combination of LDA and PIV enabled us to characterize the turbulence intensity in two directions and compute the turbulence dissipation rate. The latter quantity was determined via the longitudinal second-order structure function $D_{LL}(r)$ by assuming inertial subrange scaling $D_{LL}(r) = C_2(\varepsilon r)^{2/3}$ with a universal constant $C_2 = 2.1$ (Sreenivasan, 1995). By plotting the appropriately compensated structure function, it is possible to obtain the dissipation rate with errors on the order of 10–20%. In a recent study (de Jong et al., 2009), we found this to be the most accurate approach to determining this quantity. Table 1 gives a complete summary of the flow parameters. Improved orientation and control of the fans have allowed us to optimize the large-scale isotropy ratio of the turbulent flow, u'/v', in the center of the chamber in the range of 0.95–1.13, where u' and v' are the root-mean-square of velocity fluctuations in orthogonal directions. After the flow characterization we used holographic imaging to obtain the particle statistics with single-exposure mode and double-exposure mode for the RDF and velocity, respectively.

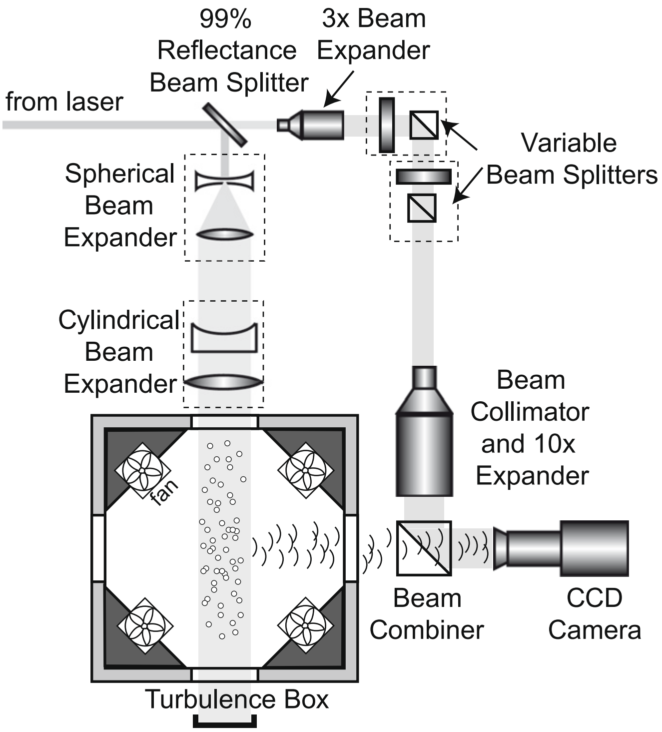

Fig. 1. Hybrid holographic digital imaging optical setup with the turbulence flow chamber.

5.2. Digital holographic imaging and reconstruction

The hybrid digital holography technique is described by Cao et al. (2008). A sketch of the holographic imaging system used in the current study is shown in Fig. 1. Only the features unique to

Table 1
Turbulent flow parameters to characterize the flow chamber.

Parameter	Value
Fan rotation rate (rpm)	3900
Turbulent kinetic energy, k ($\mathrm{m^2/s^2}$)	0.954
Turbulent intensity, u' (m/s)	0.798
Kinetic energy dissipation rate, ε ($\mathrm{m^2/s^3}$)	12.0
Large eddy length scale, $L = k^{3/2}/\varepsilon$ (cm)	7.76
Large eddy time scale, $T_e = L/u'$ (s)	0.097
Kolmogorov length scale, η (μm)	129
Kolmogorov time scale, t_η (10–3 s)	1.12
Kolmogorov velocity scale, u_η (m/s)	0.116
Taylor micro-scale, λ (mm)	3.45
Reynolds number, R_λ	184

the current system are discussed here. In order for these experiments to be consistent with Salazar et al. (2008), we used the same particles (silver-coated hollow-glass spheres with a density of 1700 kg/m^3), filtered to remove the tails of the particle size distribution (∼7 μm mean diameter, 1.9 μm standard deviation) and similar flow conditions ($St = 0.2$ and $R_\lambda = 184$). Image acquisitions were synchronized with the end of the particle injection by the addition of a National Instruments PCI-6621 timing board. The National Instruments board controlled a solenoid air valve that injected a known mass of particles (0.1 g) into the chamber over 0.5 s and then initialized the image acquisition sequence. Control of the image acquisition in this manner enabled ensemble averaging over multiple injection sequences at any given time after the particle injection. In analyzing the transient clustering process, we arbitrarily defined a phase to be a 1 s interval during the first 10 s following the particle injection. From 10 to 30 s after the injection the phases were 2 s intervals. During the last 30 s of the injection cycle (from 30 to 60 s after injection), each phase was 10 s in duration.

Two imaging setups were used in this study, one for recording the temporal and steady-state RDF and the second for measuring the particle velocities that were used to obtain the relative velocity PDF. In the first case, the imaging frame rate required for adequate temporal resolution of the evolving RDF was achieved by limiting the CCD active area to 3272 × 1224 pixels on a PCO AG, pco.4000 CCD camera (14 bit, 4008 × 2672, 9.0 μm pixel array). The lens linear magnification was set to 2.1 using a Infinity Photo-Optical Co., Model KS/2 Long-Distance Microscope lens system, which produced an effective pixel size of 4.212 μm and a view area of 13.8 × 5.1 mm^2. The depth of field was limited to 5.1 mm resulting in a total measurement volume of 359 mm^3. The frame rate of the camera was also improved by increasing the readout rate of the CCD to its fastest setting, 32 M bit s^{-1}. This combination of image size and readout rate enabled the camera to operate at 5 Hz.

For the steady-state particle relative velocity measurements we used a reduced frame rate and optimized the camera settings to maximize both the size and quality of the recorded holograms. The repetition frequency of the injection-seeded Nd:YAG laser pair was lowered to 0.33 Hz, with the double-pulse separation delay, Δt, set at 75 μs. The choice of Δt was based on the velocity scale of the flow and the accuracy of the particle position measurement. The linear magnification of the lens system was set to 4.7, and the active CCD area was set to 2650 × 2650 creating an effective pixel size of 1.921 μm and an available view area of 5.1 × 5.1 mm^2. The illuminated volume had a width of 7 mm, of which the central 5.1 mm was digitally reconstructed, resulting in a cubic measurement volume of 133 mm^3. Decreasing the effective pixel size had the effect of increasing the recording angular aperture (Meng et al., 2004) and lowering the overall noise level of the reconstructed holograms. Also, the CCD readout rate was lowered to 8 M bit s^{-1}, which maximized the dynamic range of the camera and the signal-to-noise ratio of the recorded images.

Our digital hologram processing follows the methodology of Cao et al. (2008), also described in detail by Pan (2003) and Meng et al. (2004). Briefly, the procedure involves three steps to calculate the RDF: (1) numerical reconstruction of the digital hologram to generate a reconstructed complex wave; (2) particle image segmentation from the reconstructed complex wave and (3) particle centroid localization. The numerical reconstruction algorithm uses scalar diffraction theory to numerically propagate the reference wave through the hologram. The reconstruction field involves a convolution of the hologram intensity and a diffraction kernel, implemented in the Fourier domain. "Scanning" along the axial direction is accomplished by changing the z value in the diffraction kernel (Pan and Meng, 2003).

The entire 3D reconstructed intensity field was stored in computer memory for the purpose of image segmentation, thus enabling regions to be built based on 3D connectivity relationships between adjacent foreground pixels. The principle advantage of 3D processing is that the particle extraction binarization threshold accounts for information in the entire volume, not just individual 2D reconstruction planes, which may be artificially brightened if they contain a large number of out-of-focus particle artifacts. Once the particle image is reconstructed, we estimate the 3D position of the particle by calculating the intensity-based centroid of the resulting 3D particle volume. The standard error of the depth (axial component) of the particle position was found to be ∼30 μm or 4–5 particle diameters (Cao et al., 2008). Off-axis holography has inherently better depth accuracy than in-line systems with the same magnification and is the only optical configuration usable in a large seeded facility (Pan and Meng, 2003). Significantly better depth accuracy can only be achieved with high magnifications such as those used in Sheng et al. (2006, 2008). Fig. 2 shows a sample raw hologram and the corresponding 3D particle field following the processing outlined above.

5.3. Particle velocity extraction

The double-exposure digital holograms yield two snapshots of particle positions, from which particle velocity can be extracted

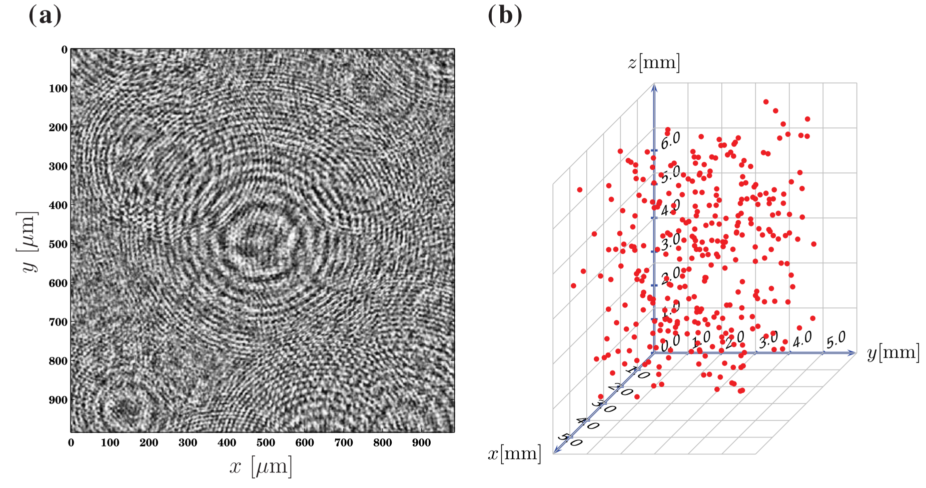

Fig. 2. An example of the 3D particle field captured by holographic imaging. (a) Sample hologram. (b) A snapshot of a 3D particle field reconstructed from a hologram demonstrating local clustering.

by comparing the positions of corresponding particles from the two sequential holographic images separated by a small time interval Δt. We used two methods to match particles between the first (A) and second (B) images: the nearest neighbor method and the relaxation method, as sketched in Fig. 3.

In the nearest neighbor algorithm, the distance between each particle in the A image and each particle in the B image is calculated. The result of this operation is a $N_A \times N_B$ matrix of distances, where N_A and N_B are the number of particles in images A and B, respectively. The initial particle match is then performed by finding the row and column of the minimum of the distance matrix. Once a particle match is obtained, the row and column containing that particle are removed from the distance matrix, reducing the matrix size to $(N_A - 1) \times (N_B - 1)$. The next minimum of the matrix is found and a new particle match is made. The row and column corresponding to the second pair are removed from the distance matrix, and the process continues until no row or column remains. Notice that the number of matched particles equals the minimum of N_A or N_B. To remove spurious pairs, the matched particle pairs are filtered by a maximum allowable distance. This distance is set to $\pm 4u'\Delta t$, where u' is the characteristic velocity scale of the flow and Δt is the pulse separation time.

In the relaxation method, a particle is matched in successive images assuming similar displacements of neighboring particles (the so-called 'quasi-rigidity' assumption). The method, described in detail in Pereira et al. (2006), can be summarized as follows. For each reference particle i located at position $\mathbf{x}_i$ in image A, a neighborhood radius R_n is defined. Under the quasi-rigidity assumption, and with some estimate for the velocity, it is possible to project the group of particles forward in time to arrive at an estimate for their positions $\tilde{\mathbf{y}}_i$ in image B. By comparing the estimate for particle i and its surrounding neighbors with the particle positions in image B within a search radius R_s of $\tilde{\mathbf{y}}_i$, the probability that particle i is matched with each particle within the search radius is estimated, taking into account the degree to which the neighboring particles match as well. A quasi-rigidity radius R_q is defined, such that only neighbors whose displacement relative to the reference particle is smaller than R_q are considered. Through an algorithm that iteratively improves the guess, the probability associated with the 'correct' particle in image B increases while the other probabilities approach zero. At the conclusion of the iterative process, particle i is matched to the particle in image B with the maximum probability. In the event that two particles in image A are matched to the same particle in image B, the match that results in the lower velocity magnitude is chosen. Whereas the nearest neighbor algorithm seeks the optimal match for each individual particle, the relaxation method optimizes the probability for the group of particles satisfying the quasi-rigidity assumption. We set $R_s = 4u'\Delta t$, $R_n = 2\eta$ and $R_q = 0.2R_s$.

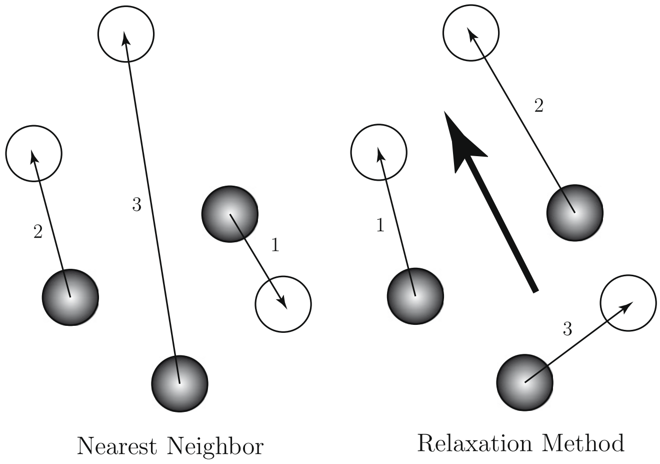

Fig. 3. Particle pairing results from the 'nearest neighbor' algorithm (left) and 'relaxation method' matching algorithm (right) for clustered particles. Black and white circles represents particles extracted from holographic images A and B, respectively. The large arrow in the relaxation method indicates the direction of the cluster motion. The numbers show the order of the pairings for each method.

6. Results and discussion

6.1. Temporal RDF

The imaging setup in Fig. 1 captured digital holograms (Fig. 2a) which were numerically reconstructed to generate the location of particles in a 3D volume (Fig. 2b). Results of the evolving RDF based on time-sequence holographic measurements are shown in Fig. 4. The two edge correction methods described in Section 3 were implemented in the RDF calculation to account for particles near the boundaries of the sample volume. Fig. 4a shows the RDF calculated by reflecting the particle field across the experimental volume at the boundaries while Fig. 4b shows the RDF calculated using the Monte Carlo approach.

It is evident that both RDF calculations approach a quasi-steady-state early in the injection cycle (5 s or 10 s after particle injection, respectively, for the two RDF approaches) that was maintained until the effect of the particle settling becomes appar-

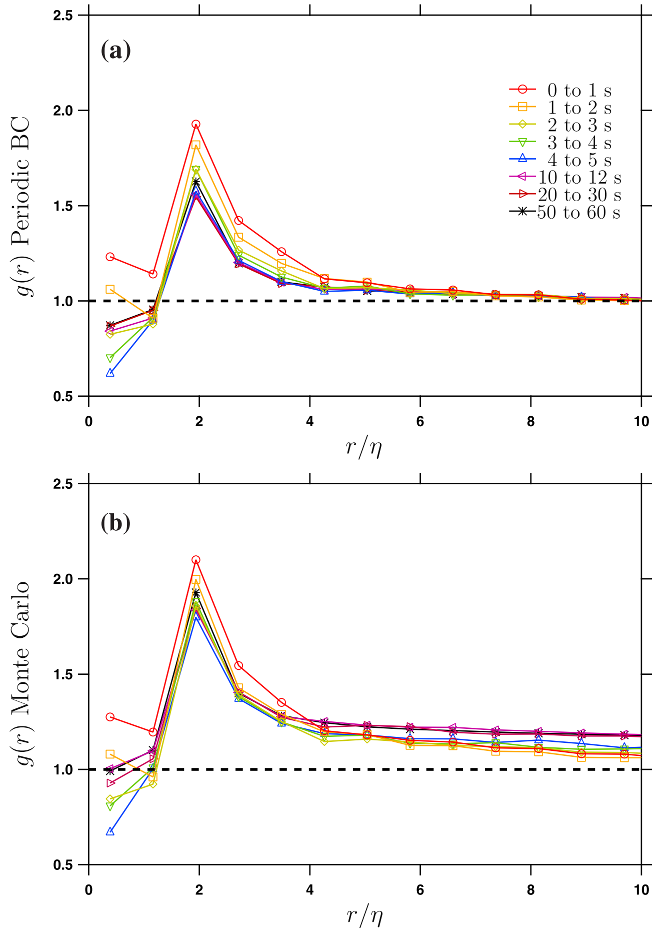

Fig. 4. Temporally evolving RDF measurements for different phases in the particle injection cycle at $St = 0.2$ using two edge correction methods: (a) periodic boundary condition and (b) Monte Carlo approach. Data is averaged over the time windows shown in the figure legend.

ent toward the end of the 60-s injection cycle. The time it takes to reach the quasi-steady state is a function of the injection methodology and the turbulent mixing process. Mixing of the particles by the turbulent flow increases the distribution of the particles over the experimental volume, lowering the RDF until a quasi-steady-state is achieved, as seen in Fig. 4. In order to better assess the effect of mixing on the temporal evolution of the RDF, we performed a DNS of inertial particles that were initially placed within a subvolume (1/64 of the total volume) in the center of the cube. The results (to be published separately) show a temporal evolution of the RDF that is qualitatively similar to the results obtained experimentally.

The difference in the time required to reach a quasi-steady-state between the two edge correction methods is related to the maximum two-particle separation distance, which is 18η with the periodic boundary condition compared to 88η for the Monte Carlo approach; i.e. as the periodic boundary condition approach uses a smaller portion of the experimental volume relative to the mixing length scale, the quasi-steady-state condition is achieved more rapidly than for the larger volume associated with the Monte Carlo approach. The difference in the effective volumes of the two methods also causes the Monte Carlo approach to produce a higher RDF at the quasi-steady-state condition due to the finite volume effect discussed earlier (see Section 3). We therefore recommend the Monte Carlo edge correction approach. The confirmation of the existence of a quasi-steady-state in our experimental system is important for the utility of the particle-laden turbulence box in studying particle statistics.

6.2. Particle radial relative velocity PDF

Particle velocities were obtained by matching individual particles in two images taken in rapid succession. We implemented the two particle matching algorithms discussed in Section 5.3 so that we could compare their performance. Once the field of particle velocities was known, we obtained relative velocities between particle pairs by subtraction, projected the resulting relative velocity vector onto the separation vector and binned the result according to the separation distance. The resulting PDFs for one particular case based on the two matching algorithms agree closely at all separation distances. This suggests that most of the group motion of particles occurs at length scales below the resolution of the experiment. The smallest separation distance for which we can accurately measure the relative velocity PDF was $r/\eta = 2.7$. At this separation, particles had only a few neighboring particles, and the group motion of particle clusters was apparently infrequent. The results we present are based on the nearest neighbor matching algorithm.

Fig. 5 shows a comparison of the experimentally measured relative velocity PDF with DNS of deterministically forced isotropic particle-laden turbulence at $R_\lambda = 147$ and $St = \{0.2, 2.0\}$. Note that the relative velocities are normalized by the Kolmogorov velocity ($u_\eta = [\nu\varepsilon]^{1/4}$) so as to make a meaningful comparison. It is evident that despite the slight mismatch in Reynolds number between the experiment and the DNS, the two PDFs are in reasonable agreement in the central region of the PDF at all separation distances. Furthermore, the broadening of the PDFs with increasing r/η are captured by both the experiment and DNS. However, the tails of the PDFs from the experiments are elevated. This may be caused by errors in the particle matching algorithm. Larger relative velocities correspond to particles undergoing larger jumps between images, which may lead to increased ambiguity in the particle matching, corrupting the statistics in the tails of the distribution. A second possibility may be physics unaccounted for in the DNS. For example, the DNS neglected gravitational settling. The discrepancy in the tails of the PDF affects the central portion of the distribution as well because by definition the PDF must integrate to unity. This may explain why the PDFs predicted by the DNS are

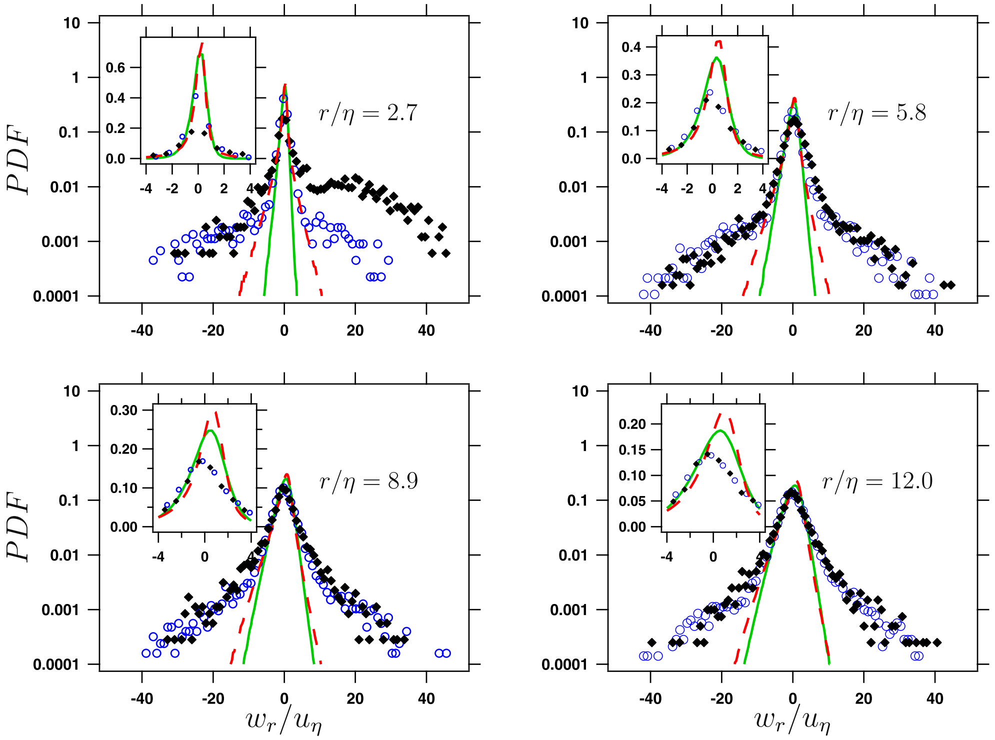

Fig. 5. Comparison of experimental (markers) and DNS (lines) radial relative velocity PDF at increasing two-particle separation distances for different *St*. In the experiment: Silver-coated hollow-glass spheres *St* = 0.2 (blue circles) and Polyimide spheres *St* = 2.4 (black diamonds). DNS values are for *St* = 0.2 (solid green line) and *St* = 2.0 (dashed red line).(For interpretation of the references to colour in this figure legend, the reader is referred to the web version of this article.)

systematically larger than the experiment in the central core (see insets in Fig. 5).

To explore if the relative velocity PDF is sensitive to the particle Stokes number, at constant Reynolds number, we repeated the experiment at the same flow condition with a larger particle (polyimide spheres, 1030 kg/m^3, ~30 μm mean diameter), thereby increasing the particle Stokes number from 0.2 to 2.4. We compare the experimentally measured relative velocity PDF for the two particles in Fig. 5 at four values of the separation distance. It is evident that the particle Stokes number does not affect the shape of the relative velocity PDF over the range of separation distances investigated in the experiment. This observation is corroborated by DNS results, which show weak sensitivity to the particle *St* within the range of the PDF available to the experiment. It is in the tails of the PDF that the *St* dependence is more pronounced, which incorporates larger experimental errors, as discussed below. For both Stokes numbers the relative velocity PDF broadens with increasing r/η, also consistent with the DNS. However, there appears to be an anomaly in the higher Stokes number case at the smallest separation, $r/\eta = 2.7$. There is a significant bump in the curve on the positive side of the abscissa axis that cannot be unequivocally explained. One possibility is that it is caused by the buildup of static charge on the surfaces of the polyimide spheres, as they are not metal coated as the smaller particles are.

Recognizing that it is the mean inward radial relative velocity that enters the expression of the collision kernel given in Eq. (1), we numerically integrate experimental and DNS PDFs at each separation distance to yield

$$\langle w_r\rangle^{(-)}(r_i) \equiv \int_{-\infty}^{0} -w_r P(w_r|r_i)dw_r. \tag{5}$$

The resulting curves for the two Stokes numbers, scaled by their respective Kolmogorov velocity, reveal an interesting crossover phenomenon, as can be seen in Fig. 6a. The explanation is as follows. At the smallest separation distances, particles of higher *St* are less correlated because of their higher inertia, resulting in a larger inward relative velocity. However, as $r/\eta \to \infty$ both particles will be decorrelated, but particles of higher *St* have less energy due to their greater inertia, resulting in a smaller relative inward velocity. The discrepancy in the quantitative values is largely due to the differences in the tails of the PDFs. This is demonstrated in Fig. 6b, which shows the same comparison as in Fig. 6a, but with the integral in Eq. (5) evaluated only over the range $-7 \leqslant w_r \leqslant 0$ for both the DNS and experiments. Notice the dramatic improvement in the agreement once the noise in the tails of the PDF has been removed. This is at least indicative of the potential quality of the comparisons between experiments and DNS that can be achieved in our system. Despite the lack of quantitative agreement, this is an encouraging comparison, and the first of its kind.

6.3. Sensitivity of the PDF to the filter width

As discussed in Section 5.3, we introduce a filter width in the nearest neighbor matching algorithm that limits the maximum speed of the particles to be less than $4u'\Delta t$. The filter is implemented to reduce the number of spurious matches between particles in the two images that are separated by a large distance. Nevertheless, the broad tails in the relative velocity PDFs suggests that incorrect matches are still occurring with the nearest neighbor algorithm. This is also evident in the sensitivity of the relative velocity PDFs to the filter width. In setting this parameter to $4u'\Delta t$, we discovered the resulting relative velocity variance and PDF could change substantially (not shown). We settled on the current filter value based on guidance from the DNS.

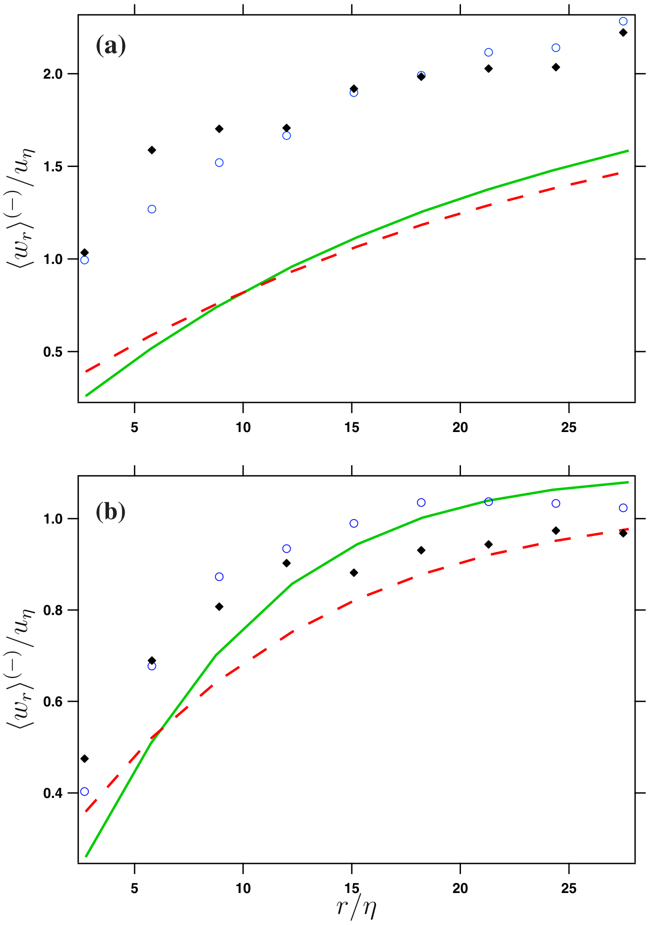

Fig. 6. Mean inward relative velocity (see Eq. (5)) comparison between DNS and experiments: (a) raw data without filtering and (b) mean inward relative velocity found by integrating the PDF over the range $-7 \leqslant w_r \leqslant 0$ for both experiment and DNS. In the experiment: Silver-coated hollow-glass spheres $St = 0.2$ (blue circles) and polyimide spheres $St = 2.4$ (black diamonds). DNS values are for $St = 0.2$ (solid green line) and $St = 2.0$ (dashed red line).(For interpretation of the references to colour in this figure legend, the reader is referred to the web version of this article.)

The issue is inherent to the problem of matching particles in the two images. The algorithms for velocity extraction from double-exposure PIV are rather mature (Adrian, 2005), but they are based on Fourier domain image correlations and thus do not provide the velocity of individual particles, as needed to study particle dynamics. Particle tracking velocimetry techniques generally track individual particles over three or more sequential images. These algorithms do not work as well when only two sequential images are involved (Ouellette et al., 2006b; Poelma et al., 2007; Poelma et al., 2006). Some algorithms first solve for the Eulerian velocity field using standard PIV correlation algorithms, and then match particles in the interrogation cells using a tracking strategy based on the underlying Eulerian fluid velocity field. However, inertial particles do not follow the fluid and hence do not provide a good estimate of the Eulerian velocity field. Therefore, double-pulsed images of inertial particle fields must rely on either basic nearest neighbor particle matching algorithms (Ouellette et al., 2006a) or more advanced cluster-matching algorithms such as the particle relaxation method or concise cross correlation to extract the particle velocities (Baek and Lee, 1996; Barnard and Thompson, 1980; Ohmi and Li, 2000; Pereira et al., 2006; Pu and Meng, 2000). The advantages of the latter approaches are only realized when the seeding density is sufficiently high for correlated motion of particle clusters to emerge. This is not the case for our system due to the competing need to keep the mass fraction sufficiently low so as to avoid significant turbulence attenuation by the particles. It appears that further study is warranted to identify optimal values for the filter as a function of the time lapse between images, Δt.

7. Conclusions

With an improved stationary isotropic turbulent flow facility and a novel hybrid holographic imaging system we have experimentally investigated the temporal development of the radial distribution function and two-particle relative velocity statistics in a particle-laden isotropic turbulent flow. While previously we have shown excellent agreement between the experimentally measured and DNS-predicted RDF that captured the inertial clustering effect (Salazar et al., 2008), this is the first time that we confirm achievement of a quasi-steady-state in the RDF, and the first time that the two-particle radial relative velocity PDF is measured with a holographic imaging system and compared with DNS. Partial agreement with the DNS is achieved, as evidenced by the strong overlap in the central portions of the PDFs. However, significant discrepancies in the tails of the PDFs remain, which we attribute to ambiguities in the matching of particles with larger velocities. Reduction of these errors will require implementation of more sophisticated particle validation algorithms such as (de Jong and Meng, 2007) and some advancement of the nearest neighbor matching algorithm, possibly through the use of multiple values of the time lapse between images.

Despite these shortcomings, the mean inward radial relative velocity results from the experiments were in good qualitative agreement with the DNS. In particular, the crossover of the curves at two values of the Stokes number with increasing r/η occurred at roughly the same separation distance. The quantitative values were not in agreement, but this is due to the elevated tails in the experimental PDFs. Despite the issues with the tails of the PDFs, the agreement over the central core of the PDF is encouraging in that holographic imaging can be used to obtain relative velocity statistics for inertial particles. The measurement of the relative velocity PDF and RDF is an indirect approach of obtaining the inertial particle collision frequency. Further refinement of the experimental technique will enable validation of the DNS as well the potential to extend the experiments to Reynolds numbers beyond the reach of current DNS.

Acknowledgements

The authors would like to acknowledge the contributions of Jun Zha for valuable discussions and assistance in data acquisition. This work was supported by the NASA Microgravity Fluid Physics Program Grants NNCO5GA45G and NNCO5GA37G, by the National Science Foundation through Grants CTS-0112514, PHY-0554675 and CBET-0756540, and by the New York State Office of Science, Technology and Academic Research (NYSTAR) under Contract No. 3538479. J.P.L.C.S. acknowledges support from the Brazilian Ministry of Education through the CAPES agency.

References

Adrian, R., 2005. Twenty years of particle image velocimetry. Experiments in Fluids 39, 159–169.

Andreani, P., Cristiani, S., 1992. The evolution of quasar clustering. The Astrophysical Journal 398, L13–L16.

Ayyalasomayajula, S., Gylfason, A., Collins, L.R., Bodenschatz, E., Warhaft, Z., 2006. Lagrangian measurements of inertial particle accelerations in grid generated wind tunnel turbulence. Physical Review Letters 97 (14), 144507.

Baek, S.J., Lee, S.J., 1996. A new two-frame particle tracking algorithm using match probability. Experiments in Fluids 22 (1), 23–32.

Barnard, S.T., Thompson, W.B., 1980. Disparity analysis of images. IEEE Transactions on Pattern Analysis and Machine Intelligence 2 (4), 333–340.

Bec, J., Biferale, L., Cencini, M., Lanotte, A., Musacchio, S., Toschi, F., 2007. Heavy particle concentration in turbulence at dissipative and inertial scales. Physical Review Letters 98, 084502.

Birouk, M., Chauveau, C., Sarh, B., Quilgars, A., Gökalp, I., 1996. Turbulence effects on the vaporization of monocomponent single droplets. Combustion Science and Technology 113 (1), 413–428.

Brenguier, J.-L., Chaumat, L., 2001. Droplet spectra broadening in cumulus clouds. Part I: Broadening in adibatic cores. Journal of the Atmospheric Sciences 58, 628–641.

Cao, L., Pan, G., de Jong, J., Woodward, S.H., Meng, H., 2008. Hybrid digital holographic imaging system for three-dimensional dense particle field measurement. Applied Optics 47 (25), 4501–4508.

Coleman, P.H., Pietronero, L., Sanders, R.H., 1988. Absence of any characteristic correlation length in the cfa galaxy catalogue. Astronomy and Astrophysics 200 (1-2), L32–L34.

Collins, L.R., Keswani, A., 2004. Reynolds number scaling of particle clustering in turbulent aerosols. New Journal of Physics 6, 119–136.

Cowen, E.A., Monismith, S.G., 1997. A hybrid digital particle tracking velocimetry technique. Experiments in Fluids 22 (3), 199–211.

Davis, M., Peebles, P.J.E., 1983. A survey of galaxy redshifts .5. The 2-point position and velocity correlations. Astrophysical Journal 267 (2), 465–482.

de Jong, J., Meng, H., 2007. Digital holographic particle validation via complex wave. Applied Optics 46, 7652–7661.

de Jong, J., Cao, L., Woodward, S., Salazar, J., Collins, L., Meng, H., 2009. Dissipation rate estimation from piv in zero-mean isotropic turbulence. Experiments in Fluids 46, 499–515.

Derevich, I.V., 2007. Coagulation kernel of particles in a turbulent gas flow. International Journal of Heat and Mass Transfer 50 (7–8), 1368–1387.

Doh, D.H., Kim, D.H., Cho, K.R., Cho, Y.B., Lee, W.J., Saga, T., Kobayashi, T., 2002. Development of genetic algorithm based 3d-ptv technique. Journal of Visualization 5 (3), 243–254.

Elsinga, G.E., Scarano, F., Wieneke, B., van Oudheusden, B.W., 2006. Tomographic particle image velocimetry. Experiments in Fluids 41 (6), 933–947.

Grassberger, P., Procaccia, I., 1983. Characterizations of strange attractors. Physical Review Letters 50, 346–349.

Hamilton, A.J.S., 1993. Toward better ways to measure the galaxy correlation-function. Astrophysical Journal 417 (1), 19–35.

Hewett, P.C., 1982. The estimation of galaxy angular correlation functions. Royal Astronomical Society, Monthly Notices 201, 867–883.

Holtzer, G.L., Collins, L.R., 2002. Relationship between the intrinsic radial distribution function for an isotropic field of particles and lower-dimensional measurements. Journal of Fluid Mechanics 459, 93–102.

Hoyer, K., Holzner, M., Luthi, B., Guala, M., Liberzon, A., Kinzelbach, W., 2005. 3d scanning particle tracking velocimetry. Experiments in Fluids 39, 923–934.

Jones, B.J.T., Martfnez, V.J., Saar, E., Trimble, V., 2005. Scaling laws in the distribution of galaxies. Reviews of Modern Physics 76 (4), 1211.

Kerscher, M., 1999. The geometry of second-order statistics – biases in common estimators. Astronomy and Astrophysics 343 (2), 333–347.

Kerscher, M., Szapudi, I., Szalay, A.S., 2000. A comparison of estimators for the two-point correlation function. Astrophysical Journal 535 (1), L13–L16.

Landy, S.D., Szalay, A.S., 1993. Bias and variance of angular-correlation functions. Astrophysical Journal 412 (1), 64–71.

Lemson, G., Sanders, R.H., 1991. On the use of the conditional density as a description of galaxy clustering. Monthly Notices of the Royal Astronomical Society 252 (3), 319–328.

Maxey, M.R., 1987. The motion of small spherical-particles in a cellular-flow field. Physics of Fluids 30 (7), 1915–1928.

McQuarrie, D.A., 1976. Statistical Mechanics. Haper and Row.

Meng, H., Pan, G., Pu, Y., Woodward, S.H., 2004. Holographic particle image velocimetry: from film to digital recording. Measurement Science and Technology 15, 673–685.

Ohmi, K., Li, H.Y., 2000. Particle-tracking velocimetry with new algorithm. Measurement Science and Technology 11 (6), 603–616.

Ouellette, N.T., Xu, H.T., Bodenschatz, E., 2006a. A quantitative study of three-dimensional lagrangian particle tracking algorithms. Experiments in Fluids 40 (2), 301–313.

Ouellette, N.T., Xu, H., Bourgoin, M., Bodenschantz, E., 2006b. Small-scale anisotropy in lagrangian turbulence. New Journal of Physics 8 (102), 1–10.

Owen, R.B., Zozulya, A.A., Benoit, M.R., Klaus, D.M., 2002. Microgravity materials and life sciences research applications of digital holography. Applied Optics 41 (19), 3927–3935.

Pan, G., 2003a. Digital holographic imaging for 3d particle and flow measurements. Ph.D. Thesis, University at Buffalo.

Pan, G., Meng, H., 2003. Digital holography of particle fields: reconstruction by use of complex amplitude. Applied Optics 42 (5), 827–833.

Pereira, F., Stuer, H., Graff, E.C., Gharib, M., 2006. Two-frame 3d particle tracking. Measurement Science and Technology 17 (7), 1680–1692.

Poelma, C., Westerweel, J., Ooms, G., 2006. Turbulence statistics from the optical whole-field measurements in particle-laden turbulence. Experiments in Fluids 40, 347–363.

Poelma, C., Westerweel, J., Ooms, G., 2007. Particle–fluid interactions in grid-generated turbulence. Journal of Fluid Mechanics 589, 315–351.

Pons-Borderia, M.J., Martinez, V.J., Stoyan, D., Stoyan, H., Saar, E., 1999. Comparing estimators of the galaxy correlation function. Astrophysical Journal 523 (2), 480–491.

Provenzale, A., Guzzo, L., Murante, G., 1994. Clustering properties from finite galaxy samples. Monthly Notices of the Royal Astronomical Society 266 (3), 555–566.

Pu, Y., Meng, H., 2000. An advanced off-axis holographic particle image velocimetry (HPIV) system. Experiments in Fluids 29, 184–197.

Ramkrishna, D., 2000. Population Balances: Theory and Applications to Particulate Systems in Engineering. Academic Press, San Diego, CA.

Reade, W., Collins, L.R., 2000. Effect of preferential concentration on turbulent collision rates. Physics of Fluids 12 (10), 2530–2540.

Salazar, J.P.L.C., De Jong, J., Cao, L.J., Woodward, S.H., Meng, H., Collins, L.R., 2008. Experimental and numerical investigation of inertial particle clustering in isotropic turbulence. Journal of Fluid Mechanics 600, 245–256.

Saw, E.W., Shaw, R.A., Ayyalasomayajula, S., Chuang, P.Y., Gylfason, A., 2008. Inertial clustering of particles in high-Reynolds-number turbulence. Physical Review Letters 100, 214501.

Sharp, N.A., 1979. Practical estimation of the angular covariance function. Astronomy and Astrophysics 74 (3), 308–312.

Shaw, R.A., 2003. Particle–turbulence interactions in atmospheric clouds. Annual Review of Fluid Mechanics 35, 183–227.

Sheng, J., Malkiel, E., Katz, J., 2006. Digital holographic microscope for measuring three-dimensional particle distributions and motions. Applied Optics 45 (16), 3893–3901.

Sheng, J., Malkiel, E., Katz, J., 2008. Using digital holographic microscopy for simultaneous measurements of 3d near wall velocity and wall shear stress in a turbulent boundary layer. Experiments in Fluids 45 (5), 1023–1035.

Sreenivasan, K., 1995. On the universality of the Kolmogorov constant. Physics of Fluids 7 (11), 2778–2784.

Sundaram, S., Collins, L.R., 1997. Collision statistics in an isotropic particle-laden turbulent suspension .1. Direct numerical simulations. Journal of Fluid Mechanics 335, 75–109.

Voth, G.A., La Porta, A., Crawford, A.M., Alexander, J., Bodenschantz, E., 2002. Measurement of particle accelerations in fully developed turbulence. Journal of Fluid Mechanics 469, 121–160.

Wang, L.P., Wexler, A.S., Zhou, Y., 1998. Statistical mechanical descriptions of turbulent coagulation. Physics of Fluids 10 (10), 2647–2651.

Wang, L.-P., Wexler, A.S., Zhou, Y., 2000. Statistical mechanical description and modelling of turbulent collision of inertial particles. Journal of Fluid Mechanics 415, 117–153.

Wood, A.M., Hwang, W., Eaton, J.K., 2005. Preferential concentration of particles in homogeneous and isotropic turbulence. International Journal of Multiphase Flow 31, 1220–1230.

Xue, Y., Wang, L.P., Grabowski, W.W., 2008. Growth of cloud droplets by turbulent collision–coalescence. Journal of the Atmospheric Sciences 65 (2), 331–356.

Xu, W., Jericho, M., Meinertzhagen, I., Kreuzer, H., 2001. Digital in-line holography for biological applications. Proceedings of the National Academy of Sciences 98 (20), 11301–11305.

Zaichik, L.I., Simonin, O., Alipchenkov, V.M., 2006. Collison rates of bidisperse inertial particles in isotropic turbulence. Physics of Fluids 18 (035110), 1–13.

Zhou, Y., Wexler, A.S., Wang, L.P., 2001. Modelling turbulent collision of bidisperse inertial particles. Journal of Fluid Mechanics 433, 77–104.